Single Phase to Ground Fault Location Method of Overhead Line Based on Magnetic Field Detection and Multi-criteria Fusion

Xiaowei Wang, Huan Du, Zhenfeng Liang, Liang Guo, Jie Gao, Mostafa Kheshti, Weibo Liu

***Abstract*—The distribution network has many branches and complex structure, and the existing protection is difficult to achieve accurate fault section location. Moreover, the monitoring device based on electrical quantity has some problems, such as high cost, power failure in installation and maintenance, and the information collected can not meet the requirements of distribution network for operation monitoring. Therefore, fault location is still a difficult problem in the existing distribution network. The magnetic field (MF) under the overhead line can reflect the change of line current, locate the fault position between two pole towers, and the magnetoresistive sensor has the advantages of low cost and uninterrupted installation and maintenance. Therefore, in recent years, the non-contact fault feeder detection and location method based on MF has begun to develop rapidly. Based on the similarity analysis of MF waveform under overhead line from different aspects by using five criteria: relative entropy, Frobenius norm, maximum mean discrepancy, cosine similarity and correlation coefficient, it proposed a multi criteria fusion fault location method based on D-S evidence theory, which makes full use of the advantages of each criterion and overcomes the limitations of single criterion. Simulation results show that the method is not affected by conductor sag, galloping and data window length, and it fit for the noise interference and high impedance fault (HIF). Compared with the other MF method, the method has stronger adaptability.**

***Index Terms*—Distribution network fault location, magnetic field, D-S evidence theory, multi criteria fusion.**

I. Introduction

WITH the rapid development of society, users have higher and higher requirements for power supply reliability. After a fault, it is necessary to accurately and quickly detect the fault location, so as to restore the stable operation of distribution network. The weak fault current of non-effective grounding system makes it difficult to locate. Statistics show that single phase to ground fault is the most common fault type leading to tripping and power failure, accounting for more than 80% of the total faults. As a direct link with users, the fast and accurate fault location of the distribution network is essential to ensure the reliability of electricity use.

A. Previous and Related Work

At present, distribution network fault location can be divided into two categories: electrical quantity-based and non electrical quantity-based. The methods based on electrical quantity are mainly divided into traveling wave, impedance-based methods and artificial intelligence [1]. The essence of traveling wave based method is the refraction and reflection of current wave and voltage wave in the line, which can be divided into single-end method [2-3] and double-end method [4]. This kind of method is widely used in the high-voltage transmission network with long radial lines. The topology of distribution network is complex, overhead lines and cables are highly mixed, and due to the short line, it requires very high equipment sampling rate, so its application is restricted. In paper [5], the arrival time of the initial fault traveling wave is determined by variational mode decomposition and teager energy operator analysis. Impedance based method needs to obtain voltage and current information and accurate line parameters. Paper [6] analyzes the phase-frequency characteristics of equivalent impedance. In paper [7], the load impedance is estimated by μPMUs, and the phase domain equations of the line is introduced to make the result more reliable. The methods based on artificial intelligence, such as neural network, have strong adaptability, but need a lot of data for training, which takes a long time and is not flexible enough. In paper [8], the energy percentage of transient voltage in each level is extracted by wavelet filter as fault feature, and then trained by neural network. In paper [9], characteristic waveform is composed of transient zero sequence current, which is trained and classified by convolutional neural network.

Methods based on non electricity include magnetic field (MF), electric field, etc. Such methods can collect line information in a non-contact manner, and a large number of installations will not lead to ferromagnetic resonance. The

This work was supported in part by the National Natural Science Foundation of China (52177114, 61403127) and Jiangxi Electric Power Co., Ltd of State Grid (521820210005, 521820220016) *(Corresponding author: Xiaowei Wang.)*

X. Wang, H. Du, Z. Liang, and W. Liu are with the School of Electrical Engineering, Xi'an University of Technology, Xi'an, 710048, China. (e-mail: proceedings@126.com, shansi2021@126.com, liang_zf@139.com).

L. Guo is with Jiangxi Electric Power Research Institute of State Grid, Nanchang, 330000, China. (e-mail: guoliangxinyu@126.com).

J. Gao is with the State Key Laboratory of Electrical Insulation and Power Equipment, Xi'an Jiaotong University, Xi'an 710049, China. (e-mail: iamgaojie1993@163.com;

M. Kheshti is with the Intelligent Control and Smart Energy Research Group, School of Engineering, the University of Warwick, Coventry, UK. (e-mail: mostafa.kheshti@warwick.ac.uk).

realization of fault location is not affected by the complex topology of the distribution network. In terms of cost, the magnetic field sensor is lower than the traditional current measuring devices, such as FTU, μPMU, fault indicator, etc. At the same time, the installation and maintenance of the sensor do not require power outages, avoiding economic losses caused by shutdown. At present, the tunnel magnetoresistive sensor has wide range and high sensitivity, in addition to, it also has small size and lower power consumption, it is good for the feature extraction of the fault information, therefore, it is suitable for the fault location of distribution network. In paper [10], the similarity of electric field waveforms of adjacent measuring points is quantified and highlighted by dynamic time warping algorithm, so as to realize the fault location of neutral non-effectively grounded system. Paper [11] measures the quasi-static electric field generated by faults, and the fault section is determined by the associated time difference of arrival of the transients. In Paper [12], an electric field detector which can realize precise time base alignment is developed. The detector can be used to locate faults, lightning and partial discharge. MF has broad application prospects and far-reaching research value in power grid state perception, fault location and energy storage [13]. In recent years, various magnetic sensors such as giant magnetoresistive sensor and tunneling magnetoresistive sensor have developed rapidly. With the advantages of low cost, high sensitivity and small volume, they will bring profound changes to the on-line monitoring of power grid [14-15]. The application of MF in fault location has become a current research hotspot. After a fault, the MF information obtained by the sensor installed at the tower will change accordingly, which can be used as the basis for fault detection and location. At this time, it is necessary to consider the distance between the conductor and the sensor, and the load imbalance, magnetic interference, sag and galloping will also affect the measurement results [16]. In paper [17], by comparing the sliding data window of 20 cycle MF, the short-circuit fault can be located quickly, but it is only suitable for the case of low grounding impedance. By introducing geometric transformation, the steady-state symmetrical component of rotating MF is obtained, and various types of faults can be located through this result [18]. Some scholars have also proposed fault location methods combining MF and traveling wave [19-20]. These methods have strong robustness, but their accuracy is highly restricted by the sampling rate of the sensor, which puts forward high requirements for the technical conditions and cost of the equipment. Paper [21] applies wavelet transform to analyze the MF, and then use variance to evaluate the average signal energy, so as to obtain the fault section. However, the selection of basis function and the decomposition layers of wavelet transform depend on human experience, and it is difficult to get accurate conclusions if it is improperly selected [22]. When dealing with high impedance fault (HIF), paper [23] obtains the MF through the sensor installed on the tower at the head end of the feeder, and uses the multiresolution morphological gradient to extract the steady-state characteristics of the signal to detect and distinguish the occurrence of HIF. Paper [24] uses the total phase shift of the high-frequency component of the MF to determine the location of tree-related HIF. In some studies, the sensor array is optimized to obtain the MF to reconstruct the current and estimate the spatial shape of the line [25-28]. In paper [29], the fault type is identified by reconstructing the polarity of the DC component in the current.

D-S evidence theory has been widely used in power grid fault detection and location, which overcomes the problem of low accuracy of a single method. Different from this paper through different algorithms to analyze the same type of objects (MF waveforms), in previous studies, the object of evidence theory fusion is often different types of electrical quantities, such as steady-state current , high-frequency transient quantity, voltage and power, or different characteristic types of the same electrical quantity, such as the amplitude and phase of the first half wave. In paper [30], the fault degree is obtained by compressed sensing algorithm and Bayesian network respectively, and then the two fault degrees are fused by evidence theory to obtain the location result. Paper [31] constructs multiple evidences based on the relationship between main protection and standby protection, and detects hidden faults in the system combined with evidence theory. Paper [32] improves the classical D-S evidence theory to make it have better effect under high conflict evidence, and takes rotating machinery as an example to verify it.

B. Problems of Existing Fault Location Methods

Although a lot of theoretical research has been done, there is still a lack of effective location methods in the actual distribution network. The difficulties faced by fault location are mainly reflected in the following two aspects:

1) For electrical quantity location methods. Due to the constraints of cost and network structure, it is difficult to obtain comprehensive real-time operation data of the line in these methods. At the same time, the algorithms for extracting fault features and analyzing and processing the features are complex, which is often difficult to apply in engineering practice. Monitoring devices of this type of method (such as ammeters and voltmeters) still have problems such as magnetic core saturation. In addition, power cut operation is required during installation and maintenance, which will affect the power consumption of users in the area.

2) For current magnetic field location methods. They simply consider the changes in the MF magnitude and direction, and the information is not fully excavated and utilized, resulting in poor adaptability and inaccurate fault location results. The combination with traveling wave is also limited by the sampling rate and cannot meet the requirements of field applications.

C. Contributions

For the problems in the above two aspects, the contributions of this paper are as follows:

1) It proposed a novel noninvasive location method based on MF. Judge whether the fault occurs in the section by comparing the similarity of MF waveforms of adjacent monitoring points. The MF is directly used to reflect the physical characteristics of the fault, and the analysis process is simple, reducing the introduction of complex algorithms for feature extraction and other steps. At the same time, the requirements for the magnetic field sensor sampling rate are not high (the frequency of several thousand Hertz can meet the needs of the location algorithm). It has great advantages in practical application.

2) It proposed a multi criteria fusion location method based on dual-axis MF component. We deeply studied the application of MF in fault location, and analyzes the MF waveform from two dimensions of *x*-axis and *y*-axis. We measured the fault information from the perspective of five criteria, which is more comprehensive and suitable for all kinds of operation conditions. D-S evidence theory is introduced to improve the fault location reliability through multi criteria fusion. The variation of MF in each axis and its influence on the method are further considered when the sag, galloping and sampling data window are different.

II. Theory Analysis

Distribution network lines can be regarded as infinite conductors, according to Biot-Savart law, the MF near the infinite long current carrying straight line can be expressed as:

$$B = \frac{\mu_0 I}{2\pi r_0} \tag{1}$$

Where μ_0 is the permeability of air, I is the current in the conductor, r_0 is the distance between the observation point and the conductor.

The power frequency electromagnetic field of the line is a quasi-static electromagnetic field, ignoring the role of geomagnetic field. The coordinate axis centered on the sensor is established. When the sensor is at different positions of the line, the MF can be approximately divided into two parts: *x*-axis and *y*-axis, as shown in Fig. 1.

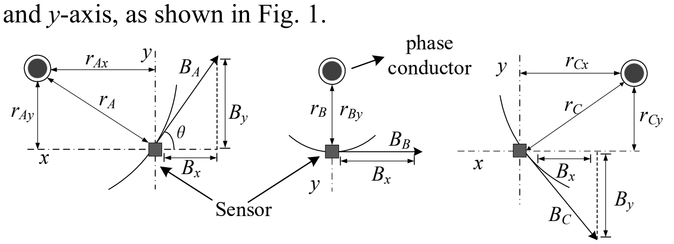

Fig. 1 Magnetic field distribution at the sensor

When the three-phase current acts alone, the MF is respectively:

$$B_A = \frac{\mu_0 I_A}{2\pi r_A} \quad B_B = \frac{\mu_0 I_B}{2\pi r_B} \quad B_C = \frac{\mu_0 I_C}{2\pi r_C} \tag{2}$$

The sum of the MF vectors at the sensor can be expressed as:

$$\begin{aligned}\vec{B} &= B_x i_x + B_y i_y + B_z i_z \\ &= \left[(B_B + B_A\cos\theta + B_C\cos\theta)i_x + (B_A\sin\theta - B_C\sin\theta)i_y + 0 i_z\right]\end{aligned} \tag{3}$$

Therefore, we can know that under different arrangements of three phase conductors, B_x points in the same direction, so the *x*-axis MF generated by the three phase conductors can be superimposed, that is, the total B_x under the overhead lines can be obtained by adding the *x*-axis components generated by the three phase conductors, the total B_x can be expressed by the calculation equation:

$$\begin{aligned}B_x &= B_A\cos\theta_A + B_B\cos\theta_B + B_C\cos\theta_C \\ &= \frac{\mu_0 I_A r_{Ay}}{2\pi r_A^2} + \frac{\mu_0 I_B r_{By}}{2\pi r_B^2} + \frac{\mu_0 I_C r_{Cy}}{2\pi r_C^2}\end{aligned} \tag{4}$$

In the three forms in Fig. 1, the different position relationship between the line and the sensor leads to the different direction of B_y. Therefore, for B_y, different arrangements of three phase conductors need to be analyzed separately and different expressions are given:

$$\begin{aligned}B_{y,\text{Horizontal}} &= B_A\sin\theta_A - B_C\sin\theta_C \\ &= \frac{\mu_0 I_A r_{Ax}}{2\pi r_A^2} - \frac{\mu_0 I_C r_{Cx}}{2\pi r_C^2}\end{aligned} \tag{5}$$

$$\begin{aligned}B_{y,\text{Vertical}} &= B_A\sin\theta_A + B_B\sin\theta_B + B_C\sin\theta_C \\ &= \frac{\mu_0 I_A r_{Ax}}{2\pi r_A^2} + \frac{\mu_0 I_B r_{Bx}}{2\pi r_B^2} + \frac{\mu_0 I_C r_{Cx}}{2\pi r_C^2}\end{aligned} \tag{6}$$

$$\begin{aligned}B_{y,\text{Triangular}} &= B_B\sin\theta_B - B_A\sin\theta_A - B_C\sin\theta_C \\ &= \frac{\mu_0 I_B r_{Bx}}{2\pi r_B^2} - \frac{\mu_0 I_A r_{Ax}}{2\pi r_A^2} - \frac{\mu_0 I_C r_{Cx}}{2\pi r_C^2}\end{aligned} \tag{7}$$

Where r_A, r_B and r_C are the distance between the three phase conductors and the sensor, r_{Ax}, r_{Bx} and r_{Cx} are the distance between the three phase conductors and the sensor on the *x*-axis, and r_{Ay}, r_{By} and r_{Cy} are the distance between the three phase conductors and the sensor on the *y*-axis respectively. i_x, i_y and i_z are the unit vectors of the *x*, *y* and *z* axes of the MF respectively. I_A, I_B and I_C are three phase currents respectively.

From equations (2) to (7), we can get that, B_x and B_y are different, and, like the current signal, the MF signal still has sinusoidal characteristics and the frequency is 50Hz.

III. Fault Location Method

A. Fault Section Location Principle

When a single phase to ground fault occurs in a 10kV distribution network, the power topology is shown in Fig. 2.

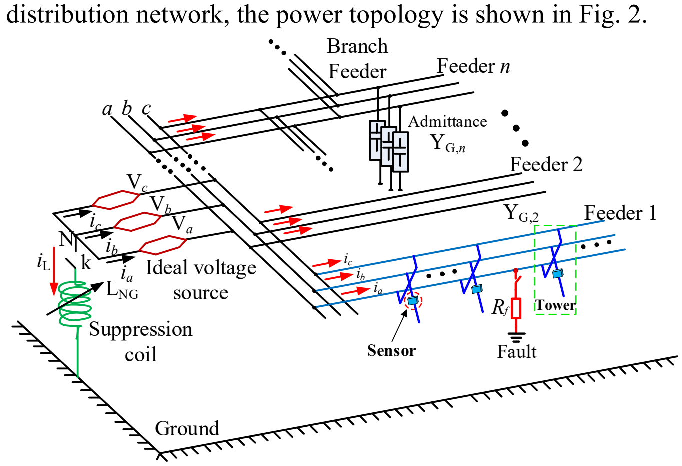

Fig. 2 Grounding fault model of distribution network

In case of single phase to ground fault, the line on the power side is connected to the earth from the fault location to form a loop, and the current flowing through the grounding point is the sum of all non-fault phase to ground capacitive currents of the system. When the grounding impedance is small, the fault phase current in front of the fault location will increase significantly, and the fault phase current behind the fault location will decrease, with significant different between them. The voltage of non fault phase increases, the phase current will also change slightly, and the current changes of two non fault phases are approximately equal. Due to the lines of the distribution network are relatively short, the current and MF remain basically unchanged on one side of the fault location. The change of three-phase current can lead to the change of MF under the overhead line. Therefore, the fault section can be determined according to the MF different on both sides of the fault location. In order to better explain this characteristic, the waveforms of fault phase current, x-axis MF and y-axis MF synthesized by three phases on both sides of the fault section are given respectively, as shown in Fig. 3.

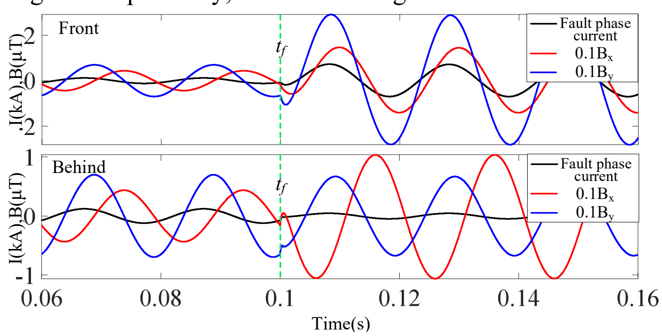

Fig. 3 Fault phase current and magnetic field waveform

When the phase currents change at the time of fault, the MF also changes sensitively. The magnetic field in front of the fault location will increase with the increase of phase current. Fig. 3 shows that the change of current will affect the MF, in other words, the change of MF can reflect the change of current. Therefore, like the current, the MF can also characterize the operation of the line.

B. *Principle of Similarity Analysis*

In this paper, five similarity analysis methods (Relative entropy, Frobenius norm, Maximum mean discrepancy, Cosine similarity and Correlation coefficient) are used to analyze the MF waveform obtained by the magnetic sensors at both ends of each section, as follows:

1) *Relative Entropy*

Relative entropy can measure the degree of uncertainty of two vectors, and the equations is the difference of information entropy between two vectors. It reflects the different between distributions from the perspective of entropy, which can be regarded as the information loss when fitting probability distribution P with probability distribution Q. It is defined as:

$$D_{KL}(P \| Q) = \sum_{i} P(i) Iog \frac{P(i)}{Q(i)} \tag{8}$$

So, relative entropy can be used to measure the approximation of MF between two adjacent monitoring points. The greater the entropy value, the greater the MF difference, that is, the greater the possibility of fault in this section, otherwise it is just the opposite. In this location algorithm, the relative entropy of the MF between the monitoring points is defined as:

$$D_{KL}(B_i \| B_{i+1}) = \left| B_{xi} Iog \frac{B_{xi}}{B_{xi+1}} \right| + \left| B_{yi} Iog \frac{B_{yi}}{B_{yi+1}} \right| \tag{9}$$

2) *Frobenius Norm*

Frobenius norm can be regarded as the Euclidean distance between matrices. It only focuses on the absolute difference of specific numerical characteristics. The size of Frobenius norm can reflect the similarity of the two matrices. For the $m \times n$ matrix **A**, its norm can be defined as:

$$\|A\|_F = \left(\sum_{i=1}^{m} \sum_{j=1}^{n} |a_{ij}|^2 \right)^{1/2} \tag{10}$$

Where, a is the element in the matrix **A**. In order to better explain the principle of Frobenius norm, assuming that the number of sampling points of the collected MF waveform is λ, the MF along the x-axis and the measured data along the y-axis at each monitoring point can form a $\lambda \times 2$ matrix $[B_x, B_y]$, the norm of the difference between the two matrices can characterize their MF similarity. Furthermore, the value of norm is inversely proportional to the similarity between the MF.

3) *Maximum Mean Discrepancy* (*MMD*)

MMD measures the distance between the source domain and target domain data in the reproducing kernel Hilbert space as the basis for judging the similarity of the distribution of two samples. The advantage of constructing a plane in a higher dimensional space to distinguish samples is that the feature space can be made complex enough to make the source domain features and the target domain features as close as possible. Assuming that X and Y are samples of two distributions, the sizes of the samples are n and m respectively, and the mapping function set is denoted by F, the empirical estimate of MMD is:

$$\mathrm{MMD}[F, X, Y] := \sup_{f \in F} \left[\frac{1}{m} \sum_{i=1}^{m} f(x_i) - \frac{1}{n} \sum_{i=1}^{n} f(y_i) \right] \tag{11}$$

Expand equations (11) to get:

$$\mathrm{MMD}[F, X, Y] = \left\| \frac{1}{n^2} \sum_{i=1}^{n} \sum_{i'=1}^{n} k(x_i, x_i') - \frac{2}{nm} \sum_{i=1}^{n} \sum_{j=1}^{m} k(x_i, y_j) + \frac{1}{m^2} \sum_{j=1}^{m} \sum_{j'=1}^{m} k(y_j, y_j') \right\|^{1/2} \tag{12}$$

In equations (12), since the mapping function is not easy to define, the process of selecting the mapping function is skipped. Generally, the Gaussian kernel $k(u,v) = e^{\frac{-\|u-v\|^2}{\sigma}}$ is used as the kernel function, and $k(x_i, x_i')$ *et al.* are directly solved.

4) *Cosine Similarity*

Cosine similarity measures the similarity between two vectors by measuring the cosine of the angle between them, and its size is between -1 and 1. Contrary to Frobenius norm, the purpose of cosine similarity is to measure the direction difference between two vectors, which is independent of the length of the vector, that is, it is insensitive to the absolute value of the specific value. It is often used to offset the high-dimensional problem of Euclidean distance. Cosine similarity has a good effect on behavior matrix discrimination. It is defined as:

$$\cos(\theta)=\frac{x \cdot y}{\|x\|\|y\|}=\frac{\sum_{i=1}^{n} x_i \times y_i}{\sqrt{\sum_{i=1}^{n}(x_i)^2} \times \sqrt{\sum_{i=1}^{n}(y_i)^2}} \tag{13}$$

Based on equation (13), the similarity between adjacent MF is defined as:

$$\cos(\theta)=\frac{\sum_{i=1}^{n-1} B_{xi} \times B_{xi+1}}{\sqrt{\sum_{i=1}^{n-1} B_{xi}^2} \times \sqrt{\sum_{i=1}^{n-1} B_{xi+1}^2}}+\frac{\sum_{i=1}^{n-1} B_{yi} \times B_{yi+1}}{\sqrt{\sum_{i=1}^{n-1} B_{yi}^2} \times \sqrt{\sum_{i=1}^{n-1} B_{yi+1}^2}} \tag{14}$$

It can be seen from equations (14) that the closer the value of cosine similarity is to 2, the more similar the MF of two adjacent monitoring points are.

5) Correlation Coefficient

The correlation coefficient is equivalent to decentralizing the data first, and further solving the cosine similarity value of the processed data. It can be regarded as an improvement of cosine similarity in the case of missing dimension value. Its calculation formula is the quotient of the covariance and standard deviation between the two variables:

$$\rho_{XY}=\frac{\operatorname{cov}(X,Y)}{\sigma_X \sigma_Y}=\frac{\sum_{i=1}^{n}(X_i-\bar{X})(Y_i-\bar{Y})}{\sqrt{\sum_{i=1}^{n}(X_i-\bar{X})^2}\sqrt{\sum_{i=1}^{n}(Y_i-\bar{Y})^2}} \tag{15}$$

Based on equation (15), the similarity between MF is defined as:

$$\rho_{i,i+1}=\frac{\sum_{i=1}^{n-1}(B_{xi}-\bar{B}_{xi})(B_{xi+1}-\bar{B}_{xi+1})}{\sqrt{\sum_{i=1}^{n-1}(B_{xi}-\bar{B}_{xi})^2}\sqrt{\sum_{i=1}^{n-1}(B_{xi+1}-\bar{B}_{xi+1})^2}} + \frac{\sum_{i=1}^{n-1}(B_{yi}-\bar{B}_{yi})(B_{yi+1}-\bar{B}_{yi+1})}{\sqrt{\sum_{i=1}^{n-1}(B_{yi}-\bar{B}_{yi})^2}\sqrt{\sum_{i=1}^{n-1}(B_{yi+1}-\bar{B}_{yi+1})^2}} \tag{16}$$

Same as cosine similarity, the closer the correlation coefficient is to 2, the more similar the MF of two adjacent monitoring points are.

C. D-S Evidence Theory

D-S evidence theory is a kind of numerical reasoning in uncertain reasoning, which can be regarded as an extension of the subjective Bayes method. D-S evidence theory can integrate the output results of multiple evidence bodies, and has a wide range of applications in expert systems, intelligence systems, multi-attribute decision analysis and other fields.

1) Basic Probability Assignment (BPA)

The recognition framework *U* of D-S evidence theory contains a limited variety of mutually exclusive results judged by each evidence body. In the location of the faulty section, that is, each section between the sensors.

The BPA on the *U* is a function m of $2^U \rightarrow [0,1]$, called the *mass* function, which represents the belief degree for *A*, which satisfies:

$$\begin{gathered} m(\varnothing)=0 \\ \sum_{A \subseteq U} m(A)=1 \end{gathered} \tag{17}$$

Where the *A* whose value is greater than 0 is called the focal element.

Relative entropy, Frobenius norm, and MMD are respectively used as an evidence body of fault location. The results obtained by the three methods are all positive values, and the larger the calculation result, the greater the difference between MF, that is, the more likely it is to be a fault section.

The *mass* functions of relative entropy, Frobenius norm and MMD are

$$m_j = D_j \Big/ \sum_{j=1}^{n-1} D_j \tag{18}$$

Where D_j is the calculation result of section *j* under a certain criterion, *j*=1, 2, 3, …, *n*-1, m_j is the fault probability of section *j* under this criterion.

In the fault location algorithm, due to the superposition calculation of dual-axis MF, the results of cosine similarity and correlation coefficient are between -2 and +2. Different from the first three criteria, the smaller the two criteria calculation results show that the greater the difference between the head and end of the section, the more likely the corresponding section is to be a fault section. So we introduced the $1/e^x$ function, as shown in Fig. 4, whose dependent variable is always greater than 0 and is a decreasing function in the entire domain. Taking equation $y=1/e^{\cos x}$ as an example, the smaller the value of cos*x*, the larger the *y* value, that is, the more likely it is a fault section. At the same time, the calculation result is always positive, which ensures the realization of the BPA.

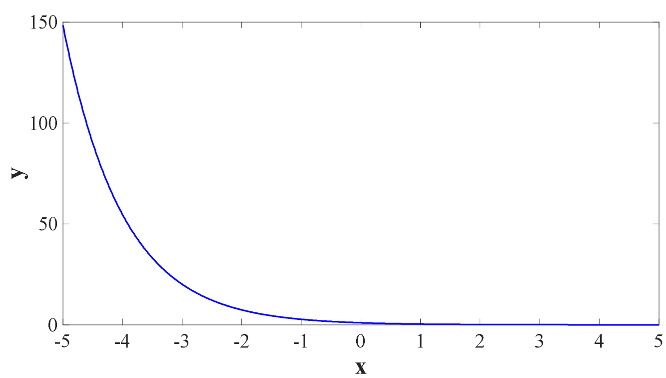

Fig. 4 $y=1/e^x$ function

The *mass* function of the two criteria of cosine similarity and correlation coefficient can be written as:

$$m'_j=\frac{1/e^{D_j}}{\sum_{j=1}^{n-1} 1/e^{D_j}} \tag{19}$$

Through the above improvements, the correlation between the degree of waveform similarity and fault probability is unified in the five criteria. Each criterion meets that the lower the similarity, the greater the probability of section fault after

BPA.

2) Dempster Composition Rule

For $\forall A \subseteq U$, the Dempster composition rule of n *mass* functions on U is

$$(m_1 \oplus m_2 \oplus \ldots \oplus m_n)(A) = \frac{1}{K} \sum_{A_1 \cap A_2 \cap \ldots \cap A_n = A} \prod_{i=1}^{n} m_i(A_i) \quad (20)$$

Where $K = \sum_{A_1 \cap A_2 \cap \cdots \cap A_n \neq \varnothing} \prod_{i=1}^{n} m_i(A_i)$ is the normalization coefficient, reflecting the degree of conflict between the various evidences, the closer the K value is to 0, the more inconsistent the judgments of the various evidences.

D. Fault Location Process

Based on similarity analysis and D-S evidence theory, the fault location process based on multi-evidence fusion is shown in Fig. 5. First, obtain the original waveform of the MF through the dual-axis magnetoresistive sensor, and the original waveform is appropriately amplified and filtered for denoising, then use five methods of relative entropy, Frobenius norm, MMD, cosine similarity, and correlation coefficient to analyze the similarity of the MF waveforms of each adjacent monitoring point. BPA based on similarity calculation result value, and the evidence theory is finally used to realize the analysis and fusion of multiple criteria.

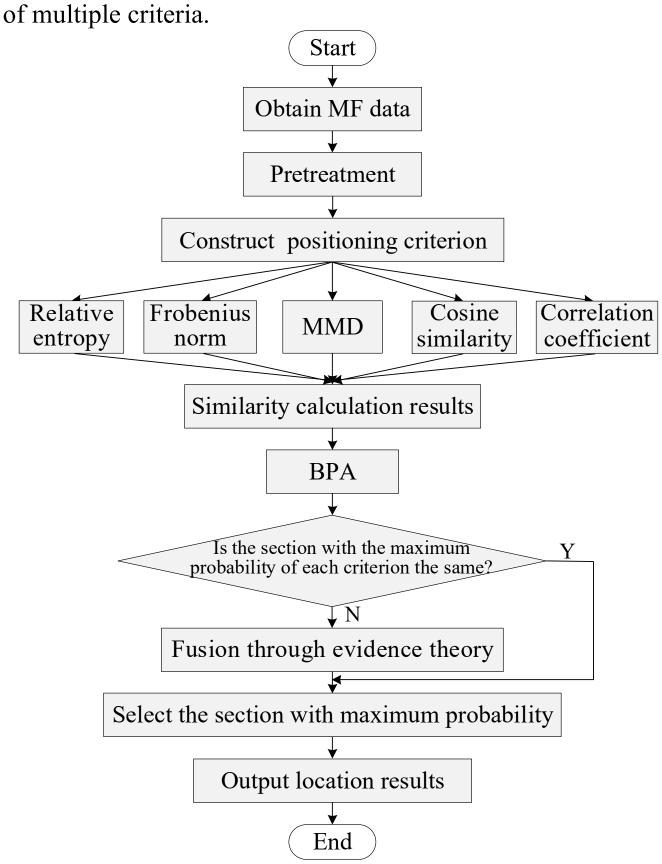

Fig. 5 Fault location process

IV. INFLUENCE FACTORS

A. Sag Influence

When considering the sag effect of the actual line, the MF at the sensor can no longer be regarded as generated by the current-carrying straight line. At this time, the line sags due to the influence of gravity and temperature, and the shape is catenary. With the increase of temperature, the horizontal stress decreases and the sag of conductor increases, resulting in the increase of MF under overhead lines. In Fig. 6, L is the span, and s is the sag. The sag curves of the three-phase conductors are all the same, that is, they have the same sag height, and the maximum sag is often in the middle of the pitch.

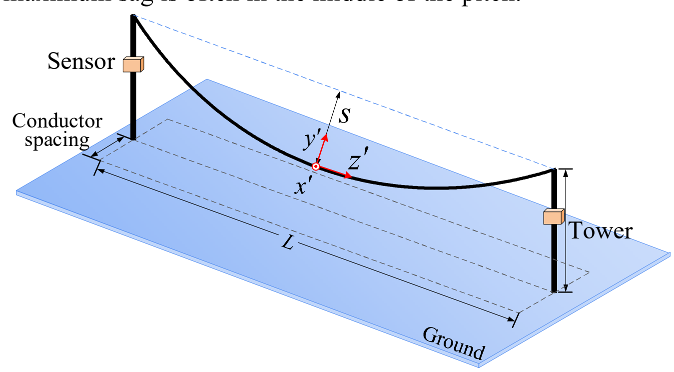

Fig. 6 Actual catenary line

As shown in Fig. 6, based on the position of the elementary current on the catenary, a coordinate system is formed, with the lowest point of the intermediate phase conductor as the origin. Combining the catenary equation and Biot-Savart law [16], we can get the MF at the sensor:

$$B_{x'} = \frac{\mu_0 I'}{4\pi} \int_{-L/2}^{L/2} \frac{\sinh(z'/a)(z_s - z') - (y_s - y')}{\left[(x_s - x')^2 + (y_s - y')^2 + (z_s - z')^2\right]^{3/2}} dz' \quad (21)$$

$$B_{y'} = \frac{\mu_0 I'}{4\pi} \int_{-L/2}^{L/2} \frac{x_s - x'}{\left[(x_s - x')^2 + (y_s - y')^2 + (z_s - z')^2\right]^{3/2}} dz' \quad (22)$$

$$B_{z'} = \frac{\mu_0 I'}{4\pi} \int_{-L/2}^{L/2} \frac{-\sinh(z'/a)(x_s - x')}{\left[(x_s - x')^2 + (y_s - y')^2 + (z_s - z')^2\right]^{3/2}} dz' \quad (23)$$

$$y' = a\left[\cosh\left(z'/a\right) - 1\right] \quad (24)$$

Where a is the catenary coefficient, which is determined by the catenary structure, I' is the phase current, x_s, y_s and z_s are the sensor coordinates in the x', y' and z' coordinate system. The line between the two sides of the pole doubles the MF of equations (21)-(23).

When the line is affected by icing or other external environments, the sag of two adjacent sections of the line will appear slightly different. Take the JM_1 pole tower as an example, the span L is 150m, when the line is regarded as horizontal straight line O, catenary O' with sag s_1 of 1.4m and catenary O'' with sag s_2 of 1.6m, the MF waveform is shown in Fig. 7.

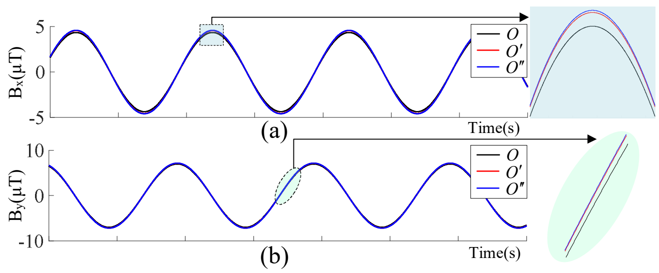

Fig. 7 Magnetic field under different sags

Considering that the ratio of MF to current is constant, B/I is set as v, therefore, $|\Delta B|$ is defined as the error between v corresponding to different MF. The calculation results are shown in Table I.

TABLE I
MAGNETIC FIELD ERROR UNDER DIFFERENT LINE SHAPES

$\lvert\Delta B\rvert$(%)	A phase	B phase	C phase
$(O-O')_x$	1.85	3.28	1.85
$(O-O'')_x$	2.11	3.76	2.11
$(O'-O'')_x$	0.27	0.50	0.27
$(O-O')_y$	2.32	0/0	2.32
$(O-O'')_y$	2.66	0/0	2.66
$(O'-O'')_y$	0.35	0/0	0.35

--0/0 indicates that the MF does not exist in both cases. (When the B phase line is directly above the sensor, the MF on the y-axis is 0.)

According to the error data in Fig. 7 and Table I, the MF considering the influence of sag is approximately equal to the MF generated by the current-carrying straight conductor, and the error does not exceed 4%. When the sag is different, the MF is basically the same, and the error is not more than 0.5%. When the sags of two adjacent sections of conductors are equal or have small differences, the MF have extremely high similarity during normal operation. Therefore, considering the actual sag does not affect the realization of the location algorithm.

B. *Influence of Conductor Galloping*

When the line is galloping due to wind blowing or uneven icing (Ignore the effect on line reactance), the wind will cause the MF distribution curve to shift towards the wind direction, and the line as a whole is approximated as being on a plane, as shown in Fig. 8, the distance between phase and phase is k, and the line is inclined towards the edge phase (phase A), s and s' are the lowest point of the line when there is no galloping and when galloping.

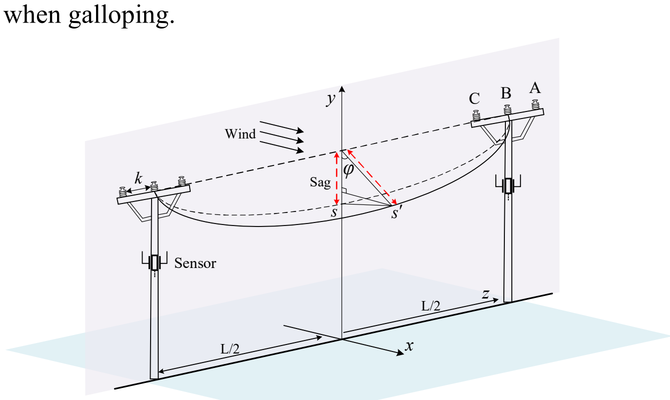

Fig. 8 Galloping line and coordinate axis plane

According to the positional relationship between the overhead line and the y-z plane in Fig. 8, the elementary current coordinate calculation formula is derived:

$$y' = s - \left\{ s - a\left[\cosh\left(z'/a\right) - 1\right] \right\} \cos\varphi \tag{25}$$

$$x' = \left\{ s - a\left[\cosh\left(z'/a\right) - 1\right] \right\} \sin\varphi \tag{26}$$

Where φ is the angle between the plane where the line is located and the y-z plane.

When the s is 1.4m and the inclination angle φ is 5°, 25°, and 50° respectively, the MF error with the inclination angle of 0° is shown in Table II.

TABLE II
MAGNETIC FIELD ERROR UNDER DIFFERENT ANGLES

$\lvert\Delta B\rvert$(%)	A Phase	B Phase	C Phase
$(O'-O'_{5°})_x$	0.2432	0.0012	0.2246
$(O'-O'_{25°})_x$	1.3664	0.0322	0.9063
$(O'-O'_{50°})_x$	2.9253	0.1227	1.1964
$(O'-O'_{5°})_y$	0.1617	0.0010/0	0.1399
$(O'-O'_{25°})_y$	0.9749	0.0049/0	0.4916
$(O'-O'_{50°})_y$	2.2414	0.0087/0	0.4236

--0.0010/0 , 0.0049/0, 0.0087/0 indicates that the v is 0.0010, 0.0049, 0.0087 at $O'_{5°}$, $O'_{25°}$, $O'_{50°}$ respectively, and is 0 at O'.

It can be seen from the data in Table II that the greater the difference between the inclination angles of two adjacent sections of lines, the MF error basically increases, but the overall difference is small. The error is not more than 3% when the inclination angle differs by 50°. Therefore, the similarity algorithm can ignore the influence of the error caused by the overhead line galloping.

C. *Influence of Different Arrangement of Phase Conductors*

When the three-phase lines are arranged differently, the installation position of the sensor is shown in Fig. 9.

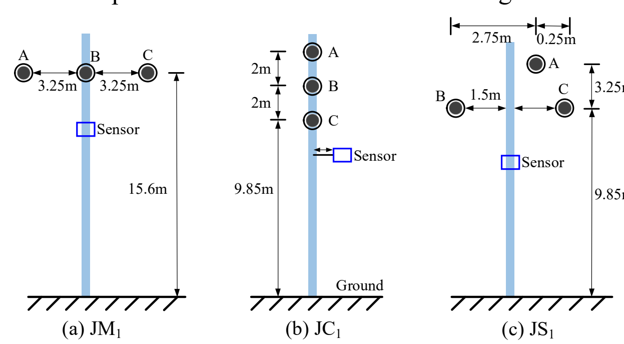

Fig. 9 Overhead line arrangement and sensor installation location

Taking a typical distribution network as an example, in Fig. 9(a), adopted horizontally arranged JM_1 pole and pole tower structure (install the sensor 3m directly below the middle phase). In Fig. 9(b), the JC_1 pole tower structure vertically arranged (the horizontal distance between the sensor and the lowest phase is 1m and the vertical distance is 2m). In Fig. 9(c), the triangular arrangement of JS_1 pole tower structure (the sensor is located in the center of B phase and C phase in the horizontal direction and 2.5m away from the lowest phase in the vertical direction). Under the three pole tower types, when the line flows through the same current, the MF distribution under the overhead line are shown in Fig. 10.

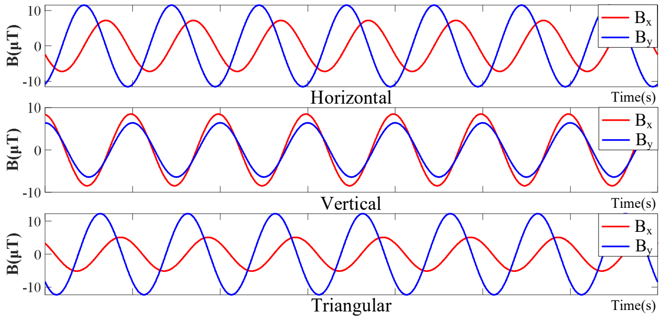

Fig. 10 Magnetic field under different conductor arrangement

Under different arrangement of three-phase lines, the amplitude and phase of MF on the same axis are different, and the difference between the two axes is also different, but their MF amplitude is close.

D. Influence of Data Window

We considered the influence of the choice of different data windows on the waveform similarity. Fig. 11 is the polar coordinate trajectory diagram of the *x*-axis and *y*-axis MF under different sampling periods.

Comparing Fig. 11(a) and Fig. 11(b), it can be seen that when a fault occurs, under the two data windows, the magnitude difference of the MF on both sides of the fault location on the same coordinate axis is basically the same. The obtained unprocessed original MF waveform is obviously more different, that is, the similarity is lower, which is more suitable for the fault location algorithm. It can be seen from Fig. 11(c) and Fig. 11(d) that the MF has stabilized during a cycle of the fault, and the MF difference remains basically unchanged.

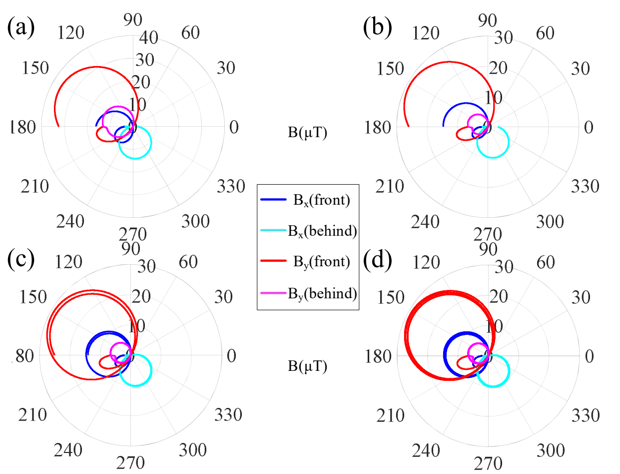

Fig. 11 Magnetic field trajectory under different data windows (a) Half cycle after fault minus the half cycle before fault (b) Half cycle after fault (c) One cycle after fault (d) 2 cycles after fault.

V. Simulation And Test Verification

A. Simulation Model

Use PSCAD to build a typical 110kV/10.5kV distribution network system, it is shown in Fig. 12. There are three overhead lines in the system, the main line is 10km, the pole tower adopts JM_1 structure, three-phase conductors are arranged horizontally, the height of the pole is 15.6m, the distance between adjacent two phases is 3.5m, the sensor is located on the pole, overcompensation degree of arc suppression coil is 5%, transformer rated capacity is 31.5MVA, sampling rate is 20kHz. f is the fault location. Table III shows the line parameters, the details are as follows:

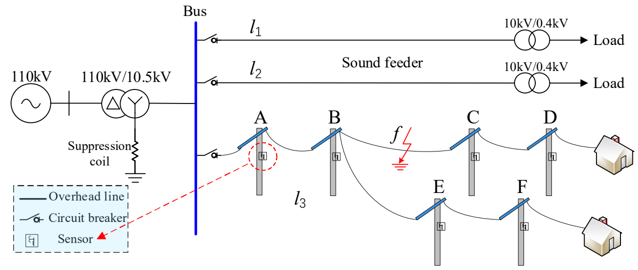

Fig. 12 10kV distribution network

TABLE III
LINE PARAMETERS

Line type	Phase sequence	R(Ω/km)	L(mH/km)	C(μF/km)
Overhead line	Positive sequence	0.170	1.210	9.700
	Zero sequence	0.230	5.480	6.000

B. Simulation Test

A-phase to ground fault occurs at location f in the BC section of line l_3 at 0.1s. We collected the second quarter cycle after the fault of each monitoring point and the third quarter cycle before the fault. Calculate each similarity criterion result according to (9) (10) (11) (14) (16) for each waveform difference. In order to facilitate the value of the Gaussian kernel sigma in MMD, the MF waveform data adopted the value when the unit is μT. The content of each row in the table is the similarity criterion, and the content of each column is the segment to be diagnosed.

1) Normal Operating Condition Test

Set the ground impedance R_f to 5Ω. It can be seen from Fig. 13 that the MF on the *x*-axis and *y*-axis on both sides of the fault location are significantly different. According to the data measured by the magnetic sensor, the similarity results of each section under each criterion are calculated, as shown in Table IV.

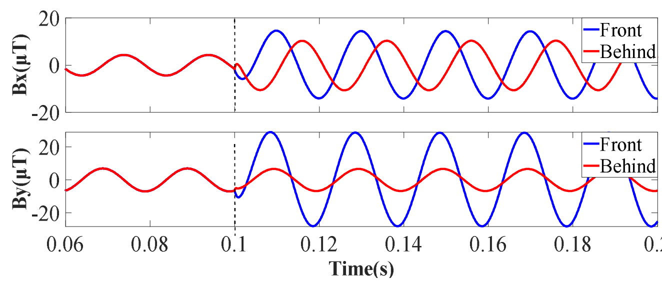

Fig. 13 Magnetic field waveform when R_f is 5Ω

TABLE IV
SIMILARITY UNDER NORMAL CONDITION

Similarity	AB	BC	CD	BE	EF
Relative entropy ($\times 10^{-7}$)	0.0138	1334.0879	0.0051	0.0081	0.0040
Frobenius norm ($\times 10^{-6}$)	0.0431	872.9902	0.0143	0.0240	0.0119
MMD($\times 10^{-4}$)	1.5463	12932.5598	0.3555	0.4236	0.1903
Cosine similarity	2.0000	-1.8207	2.0000	2.0000	2.0000
Correlation coefficient	2.0000	0.6702	2.0000	2.0000	2.0000

According to the data in Table IV, under each criterion, the similarity of the MF at both ends of the BC section is much lower than that of the other sections. From the data in Table IV and (18) (19), calculate the basic probability of each section under each criterion, which are listed in Table V.

TABLE V
BPA UNDER NORMAL CONDITION

Basic probability	AB	BC	CD	BE	EF
Relative entropy	0.0000	1.0000	0.0000	0.0000	0.0000
Frobenius norm	0.0000	1.0000	0.0000	0.0000	0.0000
MMD	0.0000	1.0000	0.0000	0.0000	0.0000
Cosine similarity	0.0201	0.9196	0.0201	0.0201	0.0201
Correlation coefficient	0.1285	0.4860	0.1285	0.1285	0.1285

For the method of applying D-S evidence theory to realize fault location, the greater the basic probability and the fusion probability value, the greater the possibility of segment fault. The basic probability of BC section under each criterion in Table V is much greater than that of other sections. It is determined that the BC section is faulty, and the result is correct. The above shows that the positioning algorithm in this paper has high reliability under the ideal condition of low grounding resistance and no interference of other external factors.

2) Noise Interference Test

In order to simulate the complex situation when the actual distribution network fault occurs, we considered the influence of noise on the location algorithm. The original MF waveform is superimposed with Gaussian white noise with a signal-to-noise ratio (SNR) of 120dB. At the same time, the grounding impedance R_f is set to 20Ω, and B_x and B_y are shown in Fig. 14.

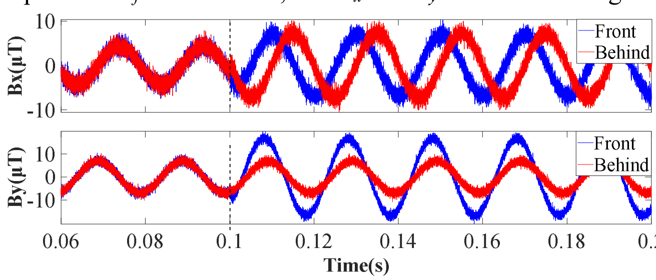

Fig. 14 Magnetic field waveform when R_f is 20Ω (SNR=120dB)

It can be seen from Fig. 14 that under this operating condition, the MF still has low similarity. Calculate the similarity results of each section under each criterion, as shown in Table VI.

TABLE VI
SIMILARITY UNDER NOISE INTERFERENCE

Similarity	AB	BC	CD	BE	EF
Relative entropy ($\times 10^{-5}$)	0.3498	4.9967	0.4510	0.4656	0.4783
Frobenius norm ($\times 10^{-5}$)	9.0980	41.6177	9.1981	8.7512	8.7742
MMD	0.0106	1.2482	0.0234	0.0122	0.0152
Cosine similarity	1.8464	-1.0441	0.8026	0.6971	0.6313
Correlation coefficient	0.5063	-0.0161	0.0947	0.0780	0.0727

According to the data in Table VI, the similarity of the MF at both ends of the BC section under each criterion is lower than that of the other sections. Table VII shows the calculated BPA.

TABLE VII
BPA UNDER NOISE INTERFERENCE

Basic probability	AB	BC	CD	BE	EF
Relative entropy	0.05188	0.74120	0.06690	0.06907	0.07095
Frobenius norm	0.11748	0.53743	0.11878	0.11301	0.11330
MMD	0.00807	0.95314	0.01783	0.00934	0.01162
Cosine similarity	0.03525	0.63459	0.10010	0.11125	0.11881
Correlation coefficient	0.13750	0.23184	0.20751	0.21102	0.21213

The data in Table VII shows that the section with the largest basic probability in each criterion is BC section, and a correct conclusion can be obtained. Therefore, from this simulation we can find the fault location method has a good anti-noise interference effect.

3) High Impedance Fault Test

The grounding impedance R_f in the above system is adjusted to 2000Ω, and the original MF waveform is superimposed with Gaussian white noise with SNR=130dB. Fig. 15 shows the MF on each axis.

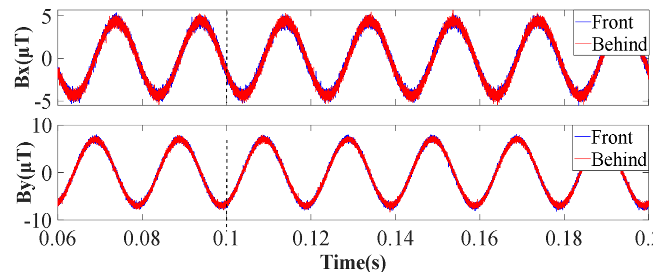

Fig. 15 Magnetic field waveform when R_f is 2000Ω (SNR=130dB)

It can be seen from Fig. 15 that the MF have a high degree of similarity under the HIF condition. The similarity of each section under each criterion are listed in Table VIII. According to the data in Table VIII, under this extreme condition, the similarity of the BC section under the first three criteria is still lower than that of other sections. Table IX shows the calculated BPA.

TABLE VIII
SIMILARITY UNDER HIGH IMPEDANCE FAULT

Similarity	AB	BC	CD	BE	EF
Relative entropy ($\times 10^{-6}$)	1.5974	1.7376	1.5416	1.6343	1.6645
Frobenius norm ($\times 10^{-5}$)	2.8181	2.9036	2.7779	2.8461	2.8660
MMD	0.0093	0.0296	0.0088	0.0066	0.0031
Cosine similarity	0.1290	-0.0505	0.0383	0.0028	-0.0697
Correlation coefficient	0.0404	-0.0393	0.0346	0.0033	-0.0726

TABLE IX
BPA UNDER HIGH IMPEDANCE FAULT

Basic probability	AB	BC	CD	BE	EF
Relative entropy	0.19539	0.21255	0.18857	0.19990	0.20359
Frobenius norm	0.19829	0.20431	0.19547	0.20026	0.20167
MMD	0.16265	0.51661	0.15286	0.11461	0.05327
Cosine similarity	0.17712	0.21194	0.19394	0.20095	0.21605
Correlation coefficient	0.19062	0.20643	0.19172	0.19782	0.21341

The maximum basic probability obtained by each criterion in Table IX is not the same section. Therefore, further fusion through evidence theory is needed, the probability of the 5 sections of line fault are: 12.61%, 58.18%, 12.42%, 10.81%, 5.98%. The probability of the BC section is much greater than that of other sections, and BC can be determined as a fault section. The results show that under this extreme condition, although there are some misjudgments of individual criteria, the integrated criterion can still accurately determine the faulty section after the fusion. The results show that the algorithm in this paper still has certain adaptability to HIF.

From the above simulation, we find that the fusion of different criteria can overcome the limitations of a single criterion and obtain a result with higher reliability than a single criterion. For example, when the single criterion of MMD is used, the maximum probability of the fault section is only 51.66%. If only the correlation coefficient analysis is applied, we may get wrong results. The simulation results of the calculation examples fully illustrate the accuracy and effectiveness of the multi-similarity criterion fault location method based on the D-S evidence theory.

4) Three Phase Unbalance Test

During the operation of distribution network, the change of load will lead to three-phase imbalance and other problems. The grounding impedance remains at 5 Ω, and the three phase loads is adjusted to different sizes. The three phase loads setting of fault feeder is shown in Table X:

TABLE X
THREE PHASE LOAD PARAMETERS

Power	A Phase	B Phase	C Phase
Active power (MW)	0.5	0.4	0.5
Reactive power (MVar)	0.03	0.03	0.04

At this time, the three-phase current and dual-axis MF are shown in the Fig. 16:

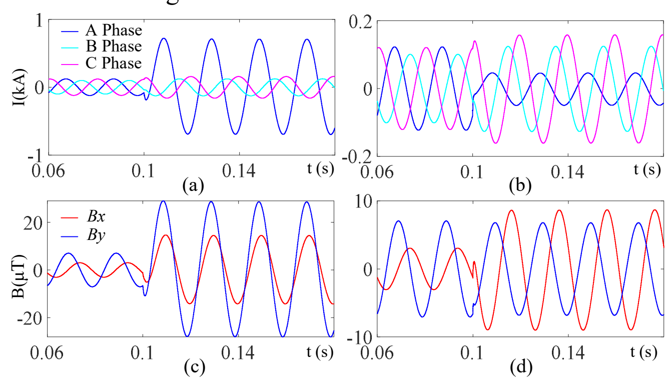

Fig. 16 Current and magnetic field waveforms under unbalanced load. (a) and (b) are the current waveforms upstream and downstream of the fault point respectively. (c) and (d) are the magnetic field waveforms upstream and downstream of the fault point respectively.

It can be seen from Fig. 16 that there are obvious differences in current and MF waveforms upstream and downstream of the fault point. The similarity calculation values of each section are shown in Table XI:

TABLE XI
SIMILARITY UNDER THREE PHASE UNBALANCE

Similarity	AB	BC	CD	BE	EF
Relative entropy ($\times 10^{-7}$)	0.0138	1333.9260	0.0050	0.0081	0.0040
Frobenius norm ($\times 10^{-6}$)	0.0431	862.7624	0.0143	0.0239	0.0118
MMD($\times 10^{-4}$)	1.5355	12899.0881	0.3443	0.3949	0.1784
Cosine similarity	2.0000	-1.8090	2.0000	2.0000	2.0000
Correlation coefficient	2.0000	0.6445	2.0000	2.0000	2.0000

It can be seen from the Table XI that when other conditions are the same, the calculated value of each criterion similarity under three-phase imbalance is very close to that under three-phase balance. As the fault section, BC is obviously different from other sections. Therefore, after BPA, the basic probability of fault section will be much greater than that of other sections, and BC section can be judged as fault section. It can be concluded that the load fluctuations will not change the characteristic that the MF waveform at the head and end of the fault section has obvious difference. At the same time, the difference between the head and end of the healthy section is still very small, so reliable positioning can still be realized in this case.

VI. FIELD DATA TESTS

In order to verify the adaptability of this method in the case of actual distribution network fault, the recording waveforms of ground fault occur in the 10kV distribution network of Changping district, Beijing, China. Three phase conductors are arranged in triangle. The fault phase is B phase and the grounding impedance is 1000 Ω. The fault occurs between section 2-3, as shown in Fig. 17:

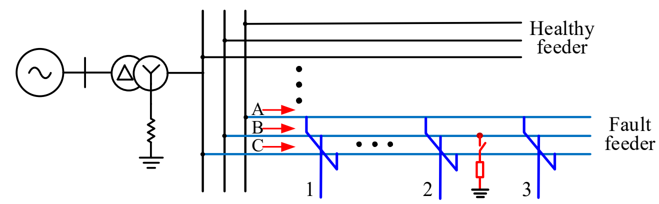

Fig. 17 Schematic diagram of fault location

The recorded current waveforms are shown in Fig. 18, and the synthetic MF waveforms are shown in Fig. 19.

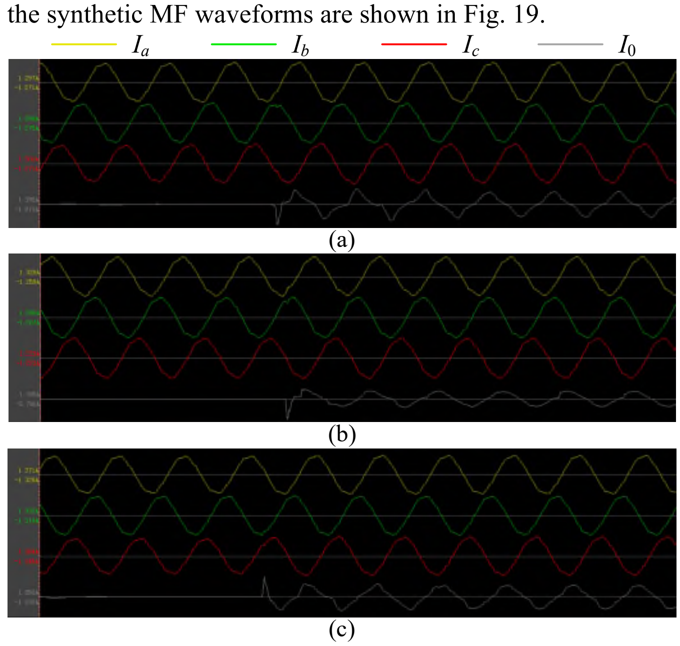

Fig. 18 Actual recording data. (a), (b) and (c) are the current waveforms of monitoring points 1, 2 and 3 respectively.

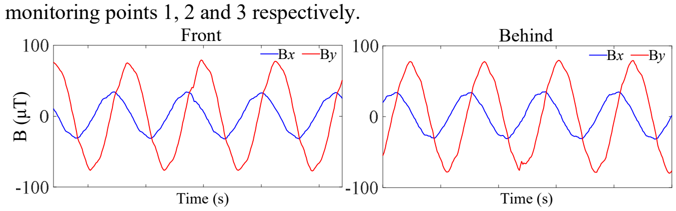

Fig. 19 Magnetic field synthesized by actual currents

It can be seen from Fig. 18 that when the grounding impedance is high, the transient component after the fault is very weak, and the difference of current between upstream and downstream of fault point is very small, resulting in some existing methods no longer feasible. In Fig. 19, the waveforms of the MF are also very similar, and it is difficult to achieve positioning only by using amplitude or phase as a criterion, so the similarity analysis algorithm needs to be used to further analyze their differences.

Calculate the similarity results of each section under each criterion, as shown in Table XII. BPA is realized based on the data in Table XII. The basic probability is shown in Table XIII:

TABLE XII
SIMILARITY CALCULATION VALUE OF EACH CRITERION

Similarity	Entropy ($\times10^{-6}$)	Norm ($\times10^{-5}$)	MMD ($\times10^{-4}$)	Cosine	Correlation coefficient
Section 1-2	4.5777	7.0500	1.5058	1.9934	1.9936
Section 2-3	10.5932	16.007	3.7160	1.9821	1.9825

TABLE XIII
BPA OF EACH CRITERION

Basic probability	Entropy	Norm	MMD	Cosine	Correlation coefficient
Section 1-2	0.3017	0.3058	0.2884	0.4972	0.4972
Section 2-3	0.6983	0.6942	0.7116	0.5028	0.5028

It can be seen from the data in the Table XII that there are obvious differences between the fault section and the healthy section, and the similarity of the fault section is lower than that of the healthy section. After BPA, as shown in Table XIII, the fault probability of the fault section under each criterion is greater than that of the healthy section, and the correct positioning results can be obtained. Therefore, in practical application, this method can still reliably realize fault location.

VII. COMPARED WITH EXISTING METHODS

The fault location method based on the comparison of MF magnitude and direction has simple algorithm and fast calculation speed, but the MF data are not fully utilized. It may not be applied under certain extreme conditions.

In case of low impedance fault, the MF magnitude on both sides of the fault location is obviously different as shown in Fig. 20, it can be compared with the threshold values to determine whether the section is faulty. The value of angle abrupt variable is used as the basis for detecting fault [20].

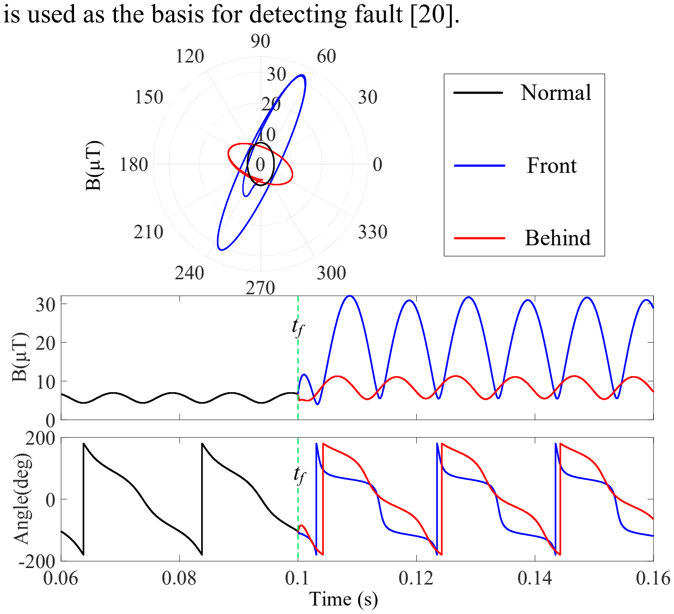

Fig. 20 Elliptical rotating of MF, absolute value and angle waveform

Fig. 21 is a diagram of the MF trajectory under different operating conditions. Under HIF, the MF trajectories are almost coincident, it is difficult to select the threshold value, and the method of comparing magnitude and direction is invalid. The elliptical trajectory of the MF presents a larger difference when it is close to the load side, which is more conducive to the realization of fault location.

In order to reflect location reliability under different severe conditions, we compared the method of this paper with the method in paper [16], and the results are shown in Table XIV.

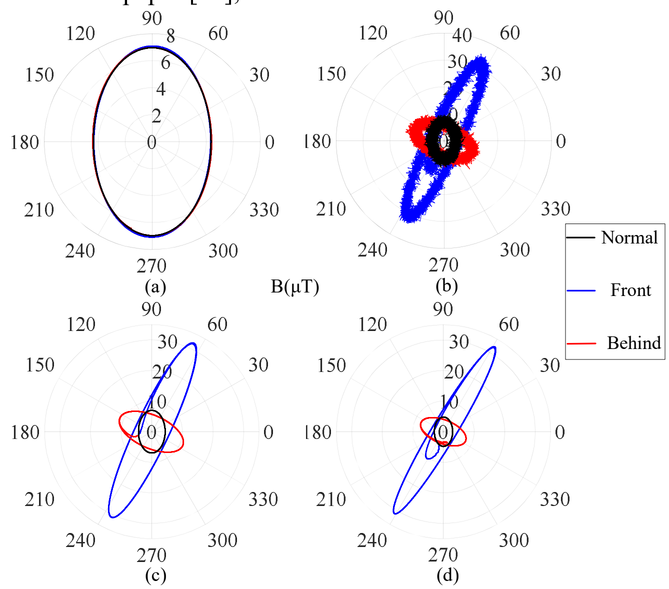

Fig. 21 Elliptical rotating of MF under different operating conditions (a) High impedance fault (b) Noise interference (c) Initial angle is 60° (d) The fault is close to the load side (section EF in Fig. 12)

TABLE XIV
LOCATION RESULTS OF DIFFERENT METHODS

Method	Criteria	R_f/Ω	SNR/ dB	Initial angles	Fault section	Numerical comparisons	√ or ×
Paper [16]	$\Delta f_v > \Delta n_v$	5	/	60°	EF	23.46>0	√
		2000	120	0°	BC	0.01<1.31	×
	180°− Δf_a<50°	5	/	60°	EF	40.96°<50°	√
		2000	120	0°	BC	172.06°>50°	×
The method	P_{max}	20	/	60°	EF	[0,0,0,0,100]	√
		2000	130	0°	BC	[13,58,12,11,6]	√

--Δf_v and Δf_a respectively is the peak difference and direction difference of the MF on both sides of the fault location, Δn_v is the peak difference of the MF on both ends of the normal section.

In case of HIF, the strong noise will greatly interfere with the magnitude comparison method, which may lead to wrong location results. The difference of initial phase angle will affect the direction based criterion. Through comparison, it can be seen that this method is more adaptive and reliable in the distribution network fault section location.

VIII. CONCLUSION

This paper proposed a fault location method for overhead lines based on the combination of MF waveform similarity and D-S evidence theory. First, it used five similarity criteria to analyze the MF waveforms from different aspects, and then, it obtained the basic probability through the criteria results, finally, it used evidence theory for fusion. The method makes full use of the advantages of each criterion, it has higher reliability than a single criterion, and improves the judgment result accuracy.

1) The method used the MF information to locate the fault, it is economical and has high accuracy. It can be located between the two pole towers and will not interfere with the line current during operation. It has the advantage of non-stop installation. Large-scale application in the distribution network has strong practical significance.

2) Although the algorithm in this paper may reduce the positioning accuracy in the absence of some monitoring device information, it can still be applied, and is not affected by three-phase imbalance and DG access (does not affect the magnetic field difference characteristics in case of fault). It has strong anti-noise ability and is suitable for HIF. It can still get high accuracy under extreme conditions.

This method has not been considered in the following aspects, and can be further studied in the future:

1) The dual-axis magnetic sensor has inherent errors such as sensitivity error and non orthogonal error, which will affect the measurement data and positioning results.

2) For the further improvement of this method, it can be used to detect fault feeder, identify fault types and so on.

3) The proportion of cable lines in urban distribution network is becoming higher and higher, using MF information to locate the fault in this condition needs further study.

4) Each similarity criterion takes different weights based on the different characteristics of different fault sections and fault types.

References

[1] K. Chen, C. Huang and J. He, Fault detection classification and location for transmission lines and distribution systems: A review on the methods, *High Voltage*, vol. 1, no. 1, pp. 25-33, Apr 2016.

[2] S. Shi, B. Zhu, A. Lei and X. Dong, Fault location for radial distribution network via topology and reclosure-generating traveling waves, *IEEE Transactions on Smart Grid*, vol. 10, no. 6, pp. 6404-6413, Nov. 2019.

[3] H. Shu, X. Liu and X. Tian, Single-ended fault location for hybrid feeders based on characteristic distribution of traveling wave along a line, *IEEE Transactions on Power Delivery*, vol. 36, no. 1, pp. 339-350, Feb. 2021.

[4] A. Tashakkori, P. J. Wolfs, S. Islam and A. Abu-Siada, Fault location on radial distribution networks via distributed synchronized traveling wave detectors, *IEEE Transactions on Power Delivery*, vol. 35, no. 3, pp. 1553-1562, June 2020.

[5] L. Xie, L. Luo, Y. Li, Y. Zhang and Y. Cao, A traveling wave-based fault location method employing VMD-TEO for distribution network, *IEEE Transactions on Power Delivery*, vol. 35, no. 4, pp. 1987-1998, Aug. 2020.

[6] X. Wang et al., Location of single phase to ground faults in distribution networks based on synchronous transients energy analysis, *IEEE Transactions on Smart Grid*, vol. 11, no. 1, pp. 774-785, Jan. 2020.

[7] H. Mirshekali, R. Dashti, A. Keshavarz, A. J. Torabi and H. R. Shaker, A novel fault location methodology for smart distribution networks, *IEEE Transactions on Smart Grid*, vol. 12, no. 2, pp. 1277-1288, Mar 2021.

[8] M. Pourahmadi-Nakhli and A. A. Safavi, Path characteristic frequency-based fault locating in radial distribution systems using wavelets and neural networks, *IEEE Transactions on Power Delivery*, vol. 26, no. 2, pp. 772-781, Apr 2011.

[9] M. F. Guo, J. H. Gao, X. Shao and D. Y. Chen, Location of single-line-to-ground fault using 1-D convolutional neural network and waveform concatenation in resonant grounding distribution systems, *IEEE Transactions on Instrumentation and Measurement*, vol. 70, pp. 1-9, 2021, Art no. 3501009.

[10] D. Xiao et al, Segment location for single-phase-to-ground fault in neutral non-effectively grounded system based on distributed electric-field measurement, *Electric Power Systems Research*, vol. 184, Article 106321, July 2020.

[11] C. Zhuang et al, Flexible noncontact approach for fault location of transmission lines using electro-optic field sensors, *IEEE Transactions on Electromagnetic Compatibility*, vol. 63, no.6, pp.2151-2158, Dec 2021.

[12] Q. Li et al, A portable electric field detector with precise time base for transient electromagnetic radiation source location, *IEEE Transactions on Instrumentation and Measurement*, vol. 69, no.4, pp.1408-1415, Apr 2020.

[13] Q. Huang, Y. Song, X. Sun, L. Jiang and P. W. T. Pong, Magnetics in smart grid, *IEEE Transactions on Magnetics*, vol. 50, no. 7, pp. 1-7, July 2014, Art no. 0900107.

[14] C. Zheng et al., Magnetoresistive sensor development roadmap (non-recording applications), *IEEE Transactions on Magnetics*, vol. 55, no. 4, pp. 1-30, Apr 2019, Art no. 0800130.

[15] C. Reig, M.-D. Cubells-Beltrán, and D. R. Munoz, Magnetic field sensors based on giant magnetoresistance (GMR) technology: Applications in electrical current sensing, *Sensors*, vol. 9, no. 10, pp. 7919–7942, Oct. 2009.

[16] Q. Huang, W. Zhen and P. W. T. Pong, A novel approach for fault location of overhead transmission line with noncontact magnetic-field measurement, *IEEE Transactions on Power Delivery*, vol. 27, no. 3, pp. 1186-1195, July 2012.

[17] M. Kazim, A. H. Khawaja, U. Zabit and Q. Huang, Fault detection and localization for overhead 11-kV distribution lines with magnetic measurements, *IEEE Transactions on Instrumentation and Measurement*, vol. 69, no. 5, pp. 2028-2038, May 2020.

[18] Đ. M. Lekić, P. D. Mršić, B. B. Erceg, Č. V. Zeljković, N. S. Kitić and P. R. Matić, Generalized approach for fault detection in medium voltage distribution networks based on magnetic field measurement, *IEEE Transactions on Power Delivery*, vol. 35, no. 3, pp. 1189-1199, June 2020.

[19] J. A. De Oliveira Neto, C. A. F. Sartori and G. M. Junior, Fault location in overhead transmission lines based on magnetic signatures and on the extended kalman filter, *IEEE Access*, vol. 9, pp. 15259-15270, 2021.

[20] K. J. Ferreira and A. E. Emanuel, A noninvasive technique for fault detection and location, *IEEE Transactions on Power Delivery*, vol. 25, no. 4, pp. 3024-3034, Oct. 2010.

[21] C. A. F. Sartori and F. X. Sevegnani, Fault classification and detection by wavelet-based magnetic signature recognition, *IEEE Transactions on Magnetics*, vol. 46, no. 8, pp. 2880-2883, Aug. 2010.

[22] X. Wang et al., High impedance fault detection method based on variational mode decomposition and teager–kaiser energy operators for distribution network, *IEEE Transactions on Smart Grid*, vol. 10, no. 6, pp. 6041-6054, Nov. 2019.

[23] M. Sarlak and S. M. Shahrtash, High-impedance faulted branch identification using magnetic-field signature analysis, *IEEE Transactions on Power Delivery*, vol. 28, no. 1, pp. 67-74, Jan. 2013.

[24] N. Bahador, F. Namdari and H. R. Matinfar, Tree-related high impedance fault location using phase shift measurement of high frequency magnetic field, *International Journal of Electrical Power & Energy Systems*, vol. 100, pp. 531-539, Sep. 2018.

[25] X. Sun, Q. Huang, Y. Hou, L. Jiang and P. W. T. Pong, Noncontact operation-state monitoring technology based on magnetic-field sensing for overhead high-voltage transmission lines, *IEEE Transactions on Power Delivery*, vol. 28, no. 4, pp. 2145-2153, Oct. 2013.

[26] X. Sun et al., Novel application of magnetoresistive sensors for high-voltage transmission-line monitoring, *IEEE Transactions on Magnetics*, vol. 47, no. 10, pp. 2608-2611, Oct. 2011.

[27] X. Sun, Q. Huang, L. J. Jiang and P. W. T. Pong, Overhead high-voltage transmission-line current monitoring by magnetoresistive sensors and current source reconstruction at transmission tower, *IEEE Transactions on Magnetics*, vol. 50, no. 1, pp. 1-5, Jan. 2014, Art no. 4000405.

[28] A. H. Khawaja, Q. Huang, J. Li and Z. Zhang, Estimation of current and sag in overhead power transmission lines with optimized magnetic field sensor array placement, *IEEE Transactions on Magnetics*, vol. 53, no. 5, pp. 1-10, May 2017, Art no. 6100210.

[29] K. Zhu and P. W. T. Pong, Fault classification of power distribution cables by detecting decaying DC components with magnetic sensing, *IEEE Transactions on Instrumentation and Measurement*, vol. 69, no. 5, pp. 2016-2027, May 2020.

[30] H. Wang et al, Method for fault location in a low-resistance grounded distribution network based on multi-source information fusion, *International Journal of Electrical Power & Energy Systems*, vol. 125, Article 106384 , Feb 2021.

[31] Z. Jiao, H. Gong and Y. Wang , A D-S evidence theory-based relay protection system hidden failures detection method in smart grid, *IEEE Transactions on Smart Grid*, vol. 9, no.3, pp.2118-2126, July 2020.

[32] Y. Lin et al, Multisensor fault diagnosis modeling based on the evidence theory, *IEEE Transactions on Reliability*, vol. 67, no. 2, pp. 513-521, June 2018.